ADVANCED FUNCTIONAL MATERIALS
www.afm-journal.de

Co(III), Co(II), Co(I): Tuning Single Cobalt Metal Atom Oxidation States in a 2D Coordination Network

*Francesco Armillotta, Davide Bidoggia, Stefania Baronio, Alessandro Sala, Roberto Costantini, Martina dell'Angela, Iulia Cojocariu, Vitaliy Feyer, Alberto Morgante, Maria Peressi, and Erik Vesselli**

It is shown that the self-assembly of a surface-confined metal–organic network such as cobalt porphyrins on graphene is accompanied by the evolution of coordination-dependent observables in the electronic structure: variation of the layer's valence states within almost 1 eV range and of the metal atoms oxidation states. Coordination of cobalt porphyrins, driven by Co ad-atoms, allows the synthesis of single metal atom centers with +3, +2, or +1 oxidation states. The electronic structure is determined by lateral interactions extending up to a few nanometers, beyond nearest-neighbor distances. The reactivity of the single Co sites, which is strongly dependent on the local electronic configuration and, thus, on the metal-specific oxidation state, is probed by carbon monoxide, which is found to ligate at pyridinic Co(I) at room temperature for background pressures above a fraction of a mbar.

1. Introduction

Surface-confined metal-organic networks (SMONs) have been intensively studied in the last two decades, representing a unique class of 2D materials with applications in catalysis, gas sensing, magnetism, and molecular storage.[1–4] The numerous combinations of metal centers and molecular tectonics provide the opportunity to finely tune the physicochemical properties of these 2D materials, controlling, e.g., coordination geometries, oxidation states of the metallic centers, density of states and electronic dispersion, work function, and HOMO-LUMO gaps.[1] While ultra-high vacuum (UHV) represents an optimal platform for the growth and for preliminarily probing such nanostructures in their as-synthesized form, bridging the UHV limits across the pressure gap allows the thorough investigation of their local chemical activity at close-to-ambient conditions,[5,6] as we will see in the following.

In this context, molecular or embedded tetracoordinated biomimetic single-metal atom sites are particularly intriguing due to their activity and stability, as observed in processes such as CO_2 electroreduction or oxygen reduction (ORR) and evolution (OER) reactions.[7–13] By interpreting porphyrins as building blocks, it is possible to assemble SMONs where single metal species coexist in non-equivalent

F. Armillotta, D. Bidoggia, S. Baronio, R. Costantini, I. Cojocariu, A. Morgante, M. Peressi, E. Vesselli
Department of Physics
University of Trieste
via A. Valerio 2, Trieste 34127, Italy
E-mail: evesselli@units.it

F. Armillotta
Institut de Physique des Nanostructures
Ecole Polytechnique Fédérale de Lausanne (EPFL)
Lausanne CH-1015, Switzerland

D. Bidoggia
Materials & Molecular Science
ICSC Italian Research Center on High Performance Computing, Big Data and Quantum Computing
Casalecchio di Reno, Bologna 40033, Italy

A. Sala, R. Costantini, M. dell'Angela, A. Morgante, E. Vesselli
CNR – Istituto Officina dei Materiali (IOM)
S.S. 14 km 163.5, Area Science Park, Basovizza, Trieste 34149, Italy

I. Cojocariu
Elettra Sincrotrone Trieste
S.C.p.A. S. S. 14, km 163.5, Trieste 34149, Italy

V. Feyer
Forschungszentrum Jülich GmbH
Peter Grünberg Institute (PGI-6)
Leo-Brandt-Straβe, 52428 Jülich, Germany

V. Feyer
Department of Physics and Center for Nanointegration Duisburg-Essen (CENIDE)
Duisburg-Essen University
47048 Duisburg, Germany

E. Vesselli
Center for Energy, Environment and Transport Giacomo Ciamician
University of Trieste
Trieste 34127, Italy

The ORCID identification number(s) for the author(s) of this article can be found under https://doi.org/10.1002/adfm.202408200

DOI: 10.1002/adfm.202408200

coordination sites,[2,14–19] as for pyridyl-substituted porphyrins (TPyPs), where one metal atom can be incorporated into the porphyrin's macrocycle (**M1**TPyPM_2), while a second one can coordinate the peripheral pyridinic-N moieties (M_1TPyP**M2** – 1d). This allows the molecules to be covalently interlinked to form an SMON. This latter specific type of metal-organic network, with $M_{1,2}$ = Fe, Co, has exhibited high electrochemical activity in OER and ORR processes,[9] and can be grown either *in vacuo* by physical vapor deposition or at the solid/liquid interface.[20,21] In both cases, µm-sized highly crystalline islands can be formed, showcasing the versatility of these nanostructures and pinpointing them as excellent candidates for in situ investigations extending across the pressure gap between UHV and *operando* conditions.[5,6,22,23]

Interestingly, Wurster et al. have demonstrated that, in the case of M_1TPyPM_2 (M_1 = Co, Fe; M_2 = –, Co, Fe) on Au(111), the electrocatalytic performance toward ORR is dramatically enhanced upon formation of the bimetallic network.[9] Specifically, the most reactive compound (CoTPyPCo) exhibits almost two orders of magnitude higher reactivity than its monometallic counterpart (CoTPyP). It remains unclear whether such behavior, not attributable to the increased (only doubled) number of potentially active sites, is solely a result of the likely different chemical identity of the two cobalt species or, as suggested, arises from a synergic cooperative interaction between the two inequivalent sites.[24]

In this study, we show how the origin of the enhanced reactivity of the CoTPyPCo nanolattice lies in the change of the oxidation states of the two inequivalent metal centers, induced by the covalent interlink of the molecules. For this purpose, we used graphene (Gr) grown on Ir(111) as support to minimize the interaction between the substrate and the SMON, thus avoiding hybridization of the single metal centers of the network with the substrate for a most conclusive analysis of the intrinsic properties of SMONs. Indeed, at variance with the Au(111) case, for the graphene-supported network, the surface trans effect is quenched, as the π-mediated weaker interaction between molecules and graphene precludes the formation of a direct bond between the substrate and the metal centers.[25–29] We investigated the role of coordination, specifically upon self-assembly of the SMON starting from the CoTPyPs monolayer, on the local and non-local electronic structure of the active sites, from monometallic CoTPyP to bimetallic CoTPyPCo, through a combination of experimental techniques and ab initio calculations. We find that the post-addition of cobalt, and the consequent SMON formation, affect (and, thus, tune) both the **Co**TPyP oxidation state and its original electronic states, resulting in an energy shift of up to 0.8 eV, depending on the adatoms/molecules coverage ratio. This means that the SMON properties can be modified by controlling the Co adatoms concentration, without the need for "external" tuning as in the case of changes to the residue's functional groups, geometric conformation of the macrocycle, alkali-metal coordination or doping, and linking architectures.[30–33] Furthermore, we observed a +1 oxidation state for the pyridinic (added) Co, which represents an unusual occurrence if we exclude systems in which substantial charge transfer is induced from the substrate.[34] Interestingly, Co(I) is addressed as the active species for various important reactions, such as CO_2 electrochemical reduction.[7,35,36] Lastly, we probe the reactivity of the two SMONs with CO. Our findings indicate that CO ligation/activation occurs exclusively at the (external) CoTPyP**Co(I)** site, with a binding energy (BE) of ≈1 eV, relevant for numerous practical catalytic applications, including CO oxidation, water gas-shift, or CO methanation.[37–39] On the basis of DFT results, we then provide a comparative analysis and explanation for why CO is selectively activated by only one of the three different CoN_4 species (**Co**TPyP, **Co**TPyPCo, CoTPyP**Co**).

2. Results

2.1. CoTPyP and CoTPyPCo Assembly Geometries

The geometric structure of the CoTPyP and CoTPyPCo monolayers on Gr/Ir(111) has been extensively described in our recent work,[40] and we provide here a concise summary of the key points. If not differently specified, the peripheral Co coverage is referred to one CoTPyP molecule (1 monolayer – ML – corresponds to one peripheral Co for each molecule). Driven by attractive lateral interactions, when deposited onto Gr/Ir(111) at 500 K, CoTPyPs form highly crystalline 2D islands. The molecules adopt the adsorption configuration illustrated in **Figure 1b**, assembling into a close-packed lattice with rectangular unit cell (1.5 × 2.8 nm^2), optimizing the interaction between the electronegative N-atoms of the pyridyl end groups and the peripheral H-atoms from the neighboring pyrrole moieties. This arrangement is typical of pyridyl-substituted porphyrins when the interaction with the substrate is weaker than the intermolecular forces, as observed on gold or silver.[41–43] The two-fold symmetry, observed in place of the expected D_4 symmetry, is attributed to the saddle shape deformation of the macrocycle.[44] Upon post-evaporation of Co ad-atoms, a rearrangement of the porphyrins' network occurs to accommodate the single Co species (Figure S1, Supporting Information). The layer becomes saturated at 1 ML coverage of peripheral Co atoms (thus, at 2 ML of total Co coverage, corresponding to 2 Co ions per molecule, including those embedded in the macrocycle). In this configuration, each single Co ad-atom is tetra-coordinated by the pyridinic terminations of adjacent CoTPyPs, as depicted in Figure 1h. The SMON can be described by a square conventional unit cell with a side of 2.9 nm, taking into account the alternating rotation of the dihedral angle of the pyridyl moieties, imparting local chirality to the layer.[40]

2.2. CoTPyP and CoTPyPCo Electronic Structure

In the initial stage of our investigation, we focus on comparing the electronic structure of the CoTPyP and CoTPyPCo metal-organic layers. We commence by analyzing scanning tunneling spectroscopy (STS) curves acquired on **Co**TPyP, **Co**TPyPCo, and CoTPyP**Co**, and dI/dV maps within the [−2, +2] V bias range (Figure 1), with the Fermi level taken as zero reference point. For CoTPyPs, the STS features (Figure 1e, green curve and marker, corresponding to the **Co**TPyP atom marked in panel b) reveal two peaks at −1.4 and +1.4 V. The corresponding spatial electronic charge distributions (Figure 1a,c) associate these features with the molecular HOMO and LUMO, respectively (the HOMO-LUMO gap for the free-standing molecule amounts to 3.24 eV).[45] While the latter is indeed centered at the Co position, exhibiting a spherical appearance, the HOMO is in fact

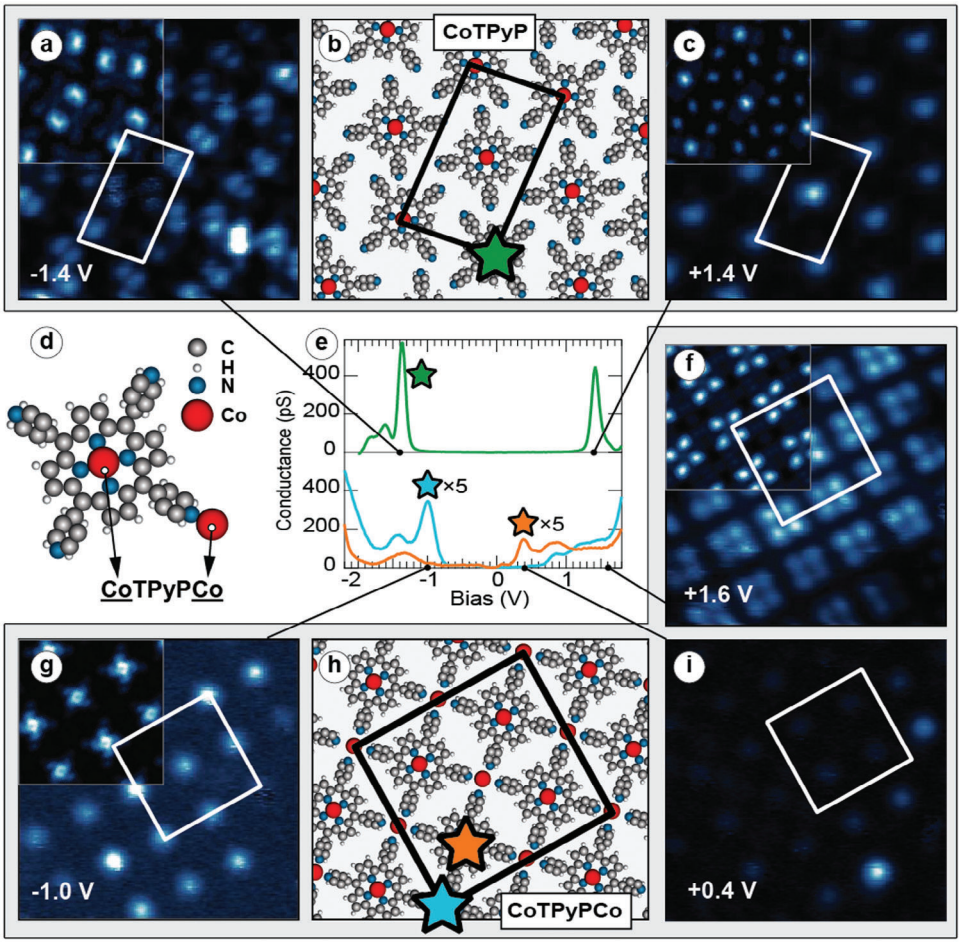

Figure 1. Scanning tunneling spectroscopy (STS) data, geometric model, and notation for CoTPyP and CoTPyPCo monolayers on Gr/Ir(111) at 77 K. a,c) dI/dV constant energy maps of the CoTPyP monolayer with corresponding DFT simulations (inset) at (a) −1.4 V and (c) +1.4 V (image size, 6 × 6 nm^2, setpoint bias voltage, +1.4 V; setpoint current, 300 pA; setpoint location, cobalt atom). b) CoTPyP adsorption geometry with rectangular conventional unit cell (1.5 × 2.8 nm^2). d) Notation and schematic chemical model used in this paper for the macrocyclic (**Co**TPyPCo) and pyridyl-coordinated (CoTPyP**Co**) single cobalt atoms. e) STS spectra acquired on the three Co species: **Co**TPyP (green), **Co**TPyPCo (orange), and CoTPyP**Co** (cyan). f,g,i) dI/dV constant energy maps of the CoTPyPCo monolayer with corresponding DFT simulations (inset) at (f) +1.6, (g) −1.0, and (i) +0.4 V (image size, 6 × 6 nm^2, setpoint bias voltage, +2.0 V; setpoint current, 50 pA; setpoint location, CoTPyP**Co**). h) CoTPyP**Co** adsorption geometry with square conventional unit cell (2.9 × 2.9 nm^2).

delocalized along the pyrrolic groups of the macrocycle. Comparison with DFT simulations, well matching the experimental data (see insets of Figure 1a,c), attributes the LUMO to the half-filled Co $3d_{z^2}$ orbital.[15,46] In the case of the CoTPyPCo layer, a significant modification of the states within this energy range is observed. The STS spectra, collected at the two Co sites of the CoTPyPCo layer (**Co**TPyPCo (cyan) and CoTPyP**Co** (orange) in Figure 1e,h), clearly indicate that the macrocyclic Co atom has undergone a change in its electronic configuration and that the two Co species are electronically and, thus, chemically inequivalent. To gain deeper insight into the nature of these differences, we systematically acquired dI/dV maps in the [−2,+2] V bias range with 0.2 V steps (see Figures S2–S7, Supporting Information for the large dataset). The analysis reveals three distinct electron spatial distributions (Figure 1f,g,i). DFT simulations are reported in the insets of the corresponding panels (f,g), showing an almost perfect match between theory and experiment. Below Fermi, a spherical state is localized at the CoTPyP**Co** sites (Figure 1g). Simulations attribute it to both Co $3d_{xz}$ and $3d_{yz}$ states (Figure S7, Supporting Information), displaying a depression at the Co site that is not resolved in the experiment. Above Fermi, a cloverleaf-shaped feature extends from +0.6 to +2.0 V (Figure 1f), centered at the CoTPyP**Co** site and mainly corresponding to states localized on the pyridyl residues.[47] A third state, about ten times less intense (refer to Figure S5, Supporting Information for intensity scale) is then resolved at +0.4 V, appearing as a bright protrusion on **Co**TPyPCo (Figure 1i). Interestingly, the CoTPyP HOMO that was previously found at −1.4 V is not observed in the bimetallic compound anymore. Our interpretation suggests that the formation of the bimetallic SMON induces a shift of ≈−1 V of this latter porphyrin state. In this scenario, the CoTPyP HOMO would shift to ≈−2.4 V, falling outside the investigated range, while the $3d_{z^2}$-based state shifts from +1.4 V (in **Co**TPyP) down to +0.4 V (in **Co**TPyPCo). This behavior is consistent with the shift of 0.6–0.7 V predicted by DFT simulations that we reported in our previous work.[40]

Before delving into the electronic structure of the saturated CoTPyPCo network, it is worth exploring the behavior of the CoTPyP layer with partial coverage of Co adatoms to investigate the coupling between the non-equivalent Co species in the SMON. We collected STS spectra of the CoTPyP**Co** unsaturated layer after 0.25 ML of Co evaporation (see Figure S8, Supporting Information). Remarkably, we observed shifts in all states with a non-linear dependence on the local Co loading and arrangement, up to 1 V for configurations differing by only a single Co atom in the surrounding coordination sphere (ranging from 0 to 8 including nearest- and next-nearest-neighbors). This result proves the role of long-range (≥ 1.5 nm) interactions between adjacent and even next-neighboring CoTPyP**Co** sites, ascribable to relatively strong magnetic super-exchange mechanisms, as previously suggested.[4,24,48,49] Whereas a more detailed investigation of this phenomenon is beyond the scope of this Article, this experimental evidence opens an exciting perspective for a deeper understanding and next-level fine-tuning of the SMON's electronic and magnetic properties.

To validate the proposed "shift hypothesis" of the electronic states, we exploited UV Photoemission Spectroscopy (UPS) to probe the occupied states within 15 eV from the Fermi level. The corresponding spectra for the CoTPyP multilayer and the CoTPyP and CoTPyPCo monolayers are reported in a. First, we identified the CoTPyP valence states at 1.5, 3.5, 7.0, and 9.0 eV BE in the CoTPyP multilayer spectra, namely for non-interacting molecules. As expected, the same resonances are observed also in the case of the single CoTPyP monolayer, due to the weak molecule-graphene interaction. Such features shift rigidly by ≈+0.8 eV after Co-coordination, witnessing an extensive change in the electronic properties. Consistently with the STS data, the new CoTPyPCo HOMO is now clearly visible at 1.0 eV. It is noteworthy to observe that all molecular states are both shifted and quenched in intensity, suggesting that they are not rigidly preserved in the formation of the coordination network, as proposed by Mandal et al.[24] The shift of the porphyrin's states is further substantiated by additional time-resolved two-photon photoelectron (2PPE) spectroscopy, as depicted in Figure S9 (Supporting Information). An excited state with a lifetime of several picoseconds is observed, above the Fermi level, for both CoTPyP mono- and multilayers, and is attributed to Q-band transitions. However, in the case of the CoTPyPCo layer, this excited state nearly vanishes. This observation aligns with the hypothesis that these macrocyclic states must shift below the Fermi level, in agreement with the picture provided so far, so that the corresponding photo-extracted electrons are concealed by those coming from the Fermi sea (thus, the transition is no longer observed).

The energy shift of the porphyrins' states induced by the formation of the SMON is associated with a change in the surface dipole, resulting in a decrease of the surface work function by as much as 0.7 eV (Figure S10, Supporting Information). That is a large quantity since it is associated with an extremely low concentration of surface Co ad-atoms (of the order of 1% with respect to the Ir substrate unit cell). This effect was not directly observed but only inferred in the case of CuTPyPCu/Au(111),[2] and was attributed to the presence of the additional, positively charged metal ad-atoms, thus decreasing the surface dipole. This finding aligns with the prediction made by DFT in our previous paper.[40] Instead, at variance with the CuTPyPCu/Au(111) case, graphene as a support completely precludes the hypothesis of the formation of a surface alloy, as proposed by Yang et al.[2]

The oxidation state of the Co species is investigated by examining the Co $2p_{3/2}$ core level using X-ray Photoemission Spectroscopy (XPS). The spectrum corresponding to the CoTPyPCo layer is shown in **Figure 2**b. It can be deconvoluted with the sum of two Doniach-Šunjic (DS) profiles centered at 781.4 and 778.6 eV BE (2.0 eV FWHM). A third convoluted profile (blue-filled in Figure 2b) takes into account uncoordinated **Co**TPyP tectons. The deconvolution parameters of the latter lineshape are obtained from our recent work, where we investigated the CoTPyP/Gr/Ir(111) Co $2p_{3/2}$ with high-energy resolution synchrotron light.[50] This profile consists of three DS envelopes centered at 784.3, 782.1, and 780.1 eV, accounting for the Co $2p_{3/2}$ multiplet splitting structure, and one at 779.4 eV, accounting for the Gunnarsson and Schönhammer (GS) transfer of the screening charge.[50–52] Thus, we attribute the peak at 778.6 eV, indicating a +1 oxidation state,[25,34,53] to CoTPyP**Co**. The feature at 781.4 eV is associated with **Co**TPyPCo and reflects the change in the valence states within the macrocycle induced by coordination with the external Co. For a cobalt-porphyrin, such a shift of ≈1.3 eV has only been observed in the presence of strongly oxidating ligands, such as NO or NO_2.[25,34] In this case, the oxidation state of Co increases from +2 to +3. The attribution of the above-mentioned Co spectroscopic features has been obtained based on the peak intensity ratios compared to the adatoms/molecules coverage ratio (0.3) and supported by our DFT simulations, which predict a +1 oxidation state for CoTPyP**Co**. The latter Co(I) is an uncommon species, known to be active, for example, toward CO_2 activation[7,35,36] and, as far as we know, it has only been observed in an SMON after non-negligible charge transfer from the substrate, as in the case of CoTPP/Cu(100).[34]

The momentum-resolved photoelectron distribution of the valence states (0 – 2.5 eV) was measured to investigate the presence of Block states delocalized on the SMON, as predicted by Mandal et al.[24] An electrostatic photoelectron emission microscope operated in the momentum mode (k-PEEM) was used, allowing the collection of photoemitted electrons in a 2D (k_x,k_y) plane image at each selected kinetic energy. The molecular states exhibit circular symmetry in the parallel momentum plane. Therefore, we present the vertical cut of the 3D data cube (energy, k_x,k_y) along the M-Γ-M direction of the graphene Brillouin zone. This direction was chosen to minimize the graphene signal that dominates around the K points. The 2D plots of the photoelectron intensity as a function of the parallel momentum (x-axis) and binding energy (y-axis) are shown in Figure 2c and d for CoTPyP and CoTPyPCo, respectively. In both cases, the signal of the bare Gr/Ir(111) has been subtracted for best evidence. Before subtraction, to compensate for the signal dampening caused by the presence of the molecular adlayer, the Gr/Ir(111) data cube intensity was affine-transformed to match the vertex of the Dirac cone. This step was necessary in order for the MOF signal to stand out from the Gr/Ir(111) background. To validate this operation, we observed that the CoTPyP and the following Co adatom depositions shift the graphene π-band downward by 6 and 34 meV, respectively (not shown), i.e., slightly relieving the mild p-doping resulting from the weak interaction with the Ir(111) substrate.[54–56] This finding demonstrates also the negligible interaction between the SMON and graphene, for even a small

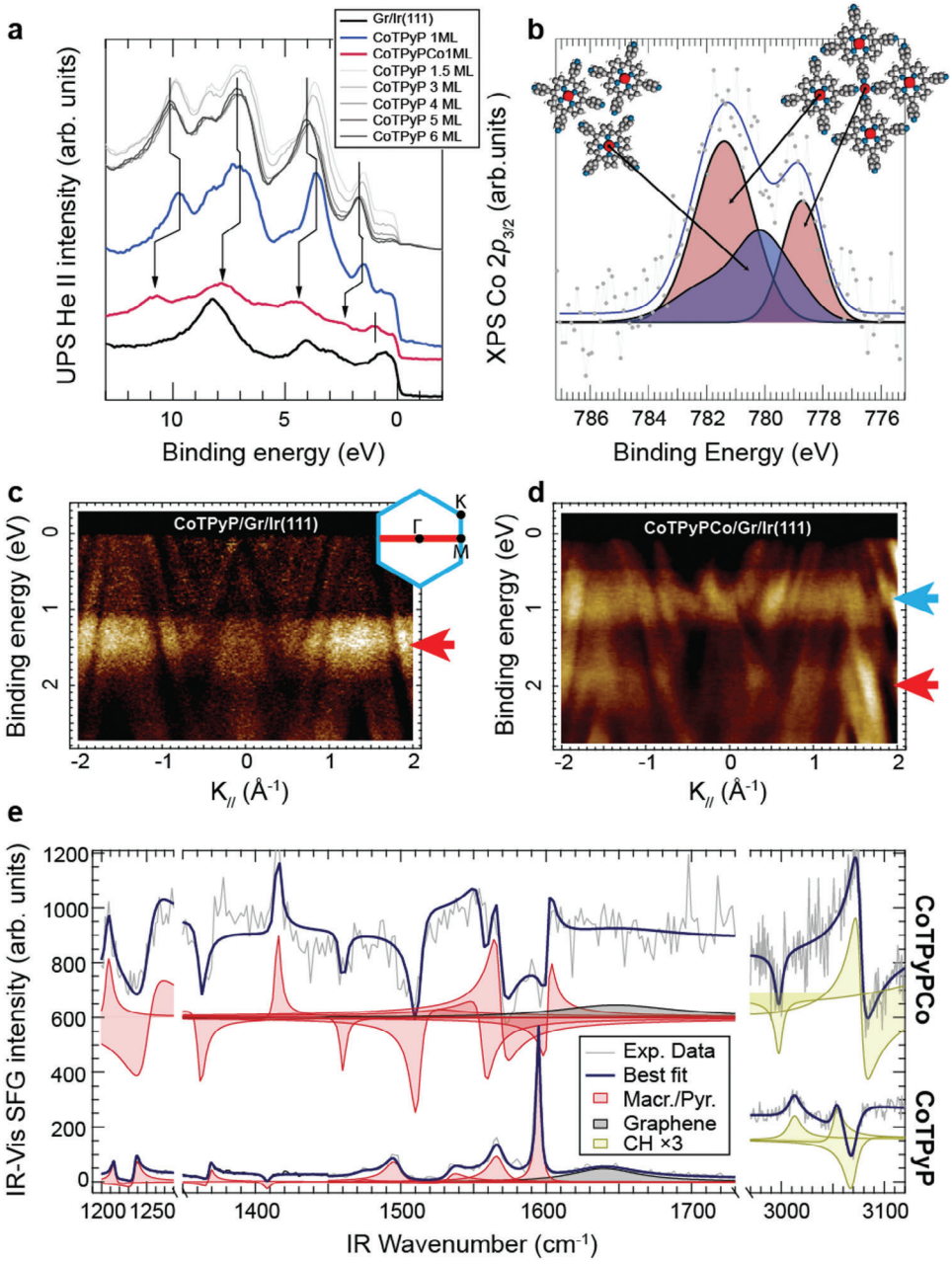

Figure 2. Multi-spectroscopic characterization of the CoTPyP and CoTPyPCo layers. a) UPS (He II) spectra of bare Gr/Ir(111), CoTPyP mono- and multilayers, and CoTPyPCo on Gr/Ir(111). The valence states shift (0.8 eV BE) between CoTPyP and CoTPyPCo cases is highlighted by the black arrows and the HOMO of CoTPyPCo is highlighted by a vertical segment at 1.0 eV BE. The curves are vertically offset for best clarity. b) Co $2p_{3/2}$ XPS experimental data (grey dots), best-fitting curves (blue solid line), and deconvolutions (filled profiles) of the CoTPyPCo monolayer. The blue-filled profile takes into account the uncoordinated **Co**TPyPs and its parameters are taken from ref.[50] (only its global amplitude was optimized on the data). c,d) Energy and parallel momentum resolved-maps along the graphene M-Γ-M direction of the (c) CoTPyP and (d) CoTPyPCo monolayers. In both cases, the Gr/Ir(111) substrate signal has been subtracted (see text). e) Normalized IR-Vis SFG experimental data (grey solid lines), with the best fitting curve (blue) and deconvolutions (filled profiles) of the two porphyrin monolayers (refer to the vertical labels). No vertical offset is applied here, putting in evidence the strong amplification of the non-resonant background upon coordination of the Co ad-atoms.

charge transfer induces important energy shifts of the graphene Dirac point.[57] In the CoTPyP/Gr/Ir(111) case (Figure 2c), the HOMO ring (orthogonal to the image plane) is measured with a radius of 1.3 $Å^{-1}$ and extends in energy from 1.0 to 1.8 eV (red arrow), in perfect agreement with STS, UPS, and literature.[58] Following the evaporation of atomic cobalt (Figure 2d), a significant change in the valence states is observed: the HOMO, previously found at 1.5 eV, has completely disappeared. On the other hand, a new HOMO appears at 0.9 eV (cyan arrow), as shown also by STS and UPS, and a less intense HOMO-1 can

be barely seen at 2.0 eV (red arrow). With the knowledge of UPS, which suggests a rigid shift of 0.8 eV of all the valence states in CoTPyPCo upon Co deposition, we can assign the HOMO-1, or more properly the SMON valence band,[24] to the former CoTPyP HOMO, shifted by ≈+0.5 eV. The new HOMO (band), instead, is attributed to the CoTPyP**Co** quasi-metallic state, and its flat appearance is the same that is observed also in the case of metallic cobalt substrates.[59,60] While no band dispersion can be resolved, the presence of highly delocalized states cannot be ruled out, yet, considering that the presence of many rotational domains (see Figure S11, Supporting Information) could have a flattening effect over the momentum space. More, the predicted band has an expected energy modulation of the order of 100 meV,[24] at the very edge of our experimental energy resolution, also in association with the strong modulation of the background due to the overlapping, intense graphene and iridium states, making the analysis extremely challenging.

In the perspective of investigating CO adsorption at near-ambient pressure, the layers have been preliminarily characterized in UHV also with InfraRed-Visible Sum-Frequency Generation (IR-Vis SFG) spectroscopy. Figure 2e shows the normalized IR-Vis SFG data for the CoTPyP and CoTPyPCo layers with the corresponding fitting curves and deconvolution profiles (see Table S1, Supporting Information for fitting parameters). In both systems, molecular vibrations are detected, together with the graphene optical G mode (which is blue-shifted up to 1640 cm^{-1}).[61] For the CoTPyPs, we attribute the two resonances at 1214 and 1595 cm^{-1} to the symmetric and antisymmetric stretching of the pyridinic moieties, respectively.[62–65] All other resonances originate from macrocyclic internal stretching and deformations.[29,65] Between 2970 and 3120 cm^{-1}, we observe the C—H stretching contributions coming from both the macrocycle and pyridinic groups. Following cobalt evaporation, the first observation is the dramatic increase in the non-resonant background amplitude, up to a factor of 10^2. Such an increase can be related to the change in the electronic structure described so far. In a simple picture, the smaller HOMO-LUMO energy gap in CoTPyPCo (˜1 eV compared to 2.3 eV of CoTPyP, from Figure 1e) increases the number of joint-density of states available for the electronic transition in the SFG process, provided that the visible photon energy here used is 2.33 eV.[66–68] The second observation is the Co-induced energy shifts (of the order of 10 cm^{-1}) of the pyridinic resonances, directly bonded to the external Co, and of the other macrocycle-related resonances. This further suggests that the SMON formation affects also the macrocyclic electronic and bonding structure.

2.3. CO Activation on Pyridinic Co

We then exploited carbon monoxide as a ligand to locally probe the reactivity of the three cobalt species: **Co**TPyP, **Co**TPyPCo, and CoTPyP**Co**. The layers, as prepared in UHV, were exposed to a static CO background up to 5×10^{-3} mbar at room temperature, without breaking the vacuum. The corresponding IR-Vis-SFG spectra, collected in situ in the CO stretching region, are reported in **Figure 3**.

In the case of the CoTPyP monolayer, the absence of any resonance indicates that there is no carbonylation of any site. Conversely, after coordination of the SMON with the Co ad-atoms, two resonances appear at 1949 and 1965 cm^{-1}, under the same pressure and temperature conditions. These vibronic modes are attributed to the internal stretch of the CO molecule ligated in terminal configuration (on-top, monocoordinated site). Both modes belong to the same chemical species: the component at 1965 cm^{-1} is ascribed to the fundamental SFG transition (red-filled profile in Figure 3), involving the vibrational excitation of CO from the fundamental to the first excited state (ω_{01}). The intense IR pulse energy (≈250 µJ with ≈30 ps duration) induces also the transition from the first to the second excited state (ω_{12}), associated with the resonance at 1949 cm^{-1} (green-filled profile in Figure 3). The energy difference is due to the anharmonicity of the C—O intra-molecular potential. Accordingly, we observe that the amplitude ratio of the two resonances changes with the power of the IR pulses, with higher intensity in the fundamental transition mode for lower IR power (Figure S12, Supporting Information), thus supporting our assignment. To our knowledge, this is the first instance of observing the hot band in the case of CO ligation in a metal atom coordination network. The anharmonic coefficient χ_e of the C—O intra-potential can be measured with the following relation:[69]

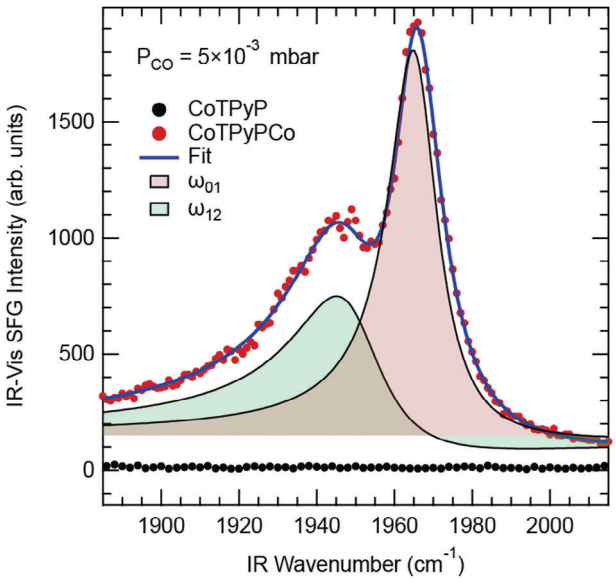

Figure 3. CO activation. Normalized IR-Vis SFG spectra of the internal C—O stretching energy region collected in situ in 5×10^{-3} mbar CO at room temperature (corresponding to saturation of the Co sites) for the CoTPyP and CoTPyPCo monolayers. The best fitting curve (blue solid line) is plotted together with the two deconvolutions (filled profiles; ω_{01} = 1965 cm^{-1}, $\Delta\varphi_{01}$ = 290°, Γ_{01} = 2.6 cm^{-1}; ω_{12} = 1949 cm^{-1}, $\Delta\varphi_{12}$ = 330°, Γ_{12} = 6.5 cm^{-1}).

$$\chi_e = \frac{\omega_{01} - \omega_{12}}{2\omega_{01}} \quad (1)$$

We obtain χ_e = 0.005, close to the values ≈0.007 previously measured for CO/Ru(0001) or CO/Ir(111).[69,70] In the case of the CoTPyPCo layer, we mention that CO ligation at room temperature is reversible: the pristine layer vibrational fingerprints are restored upon pumping out the CO background and recovering

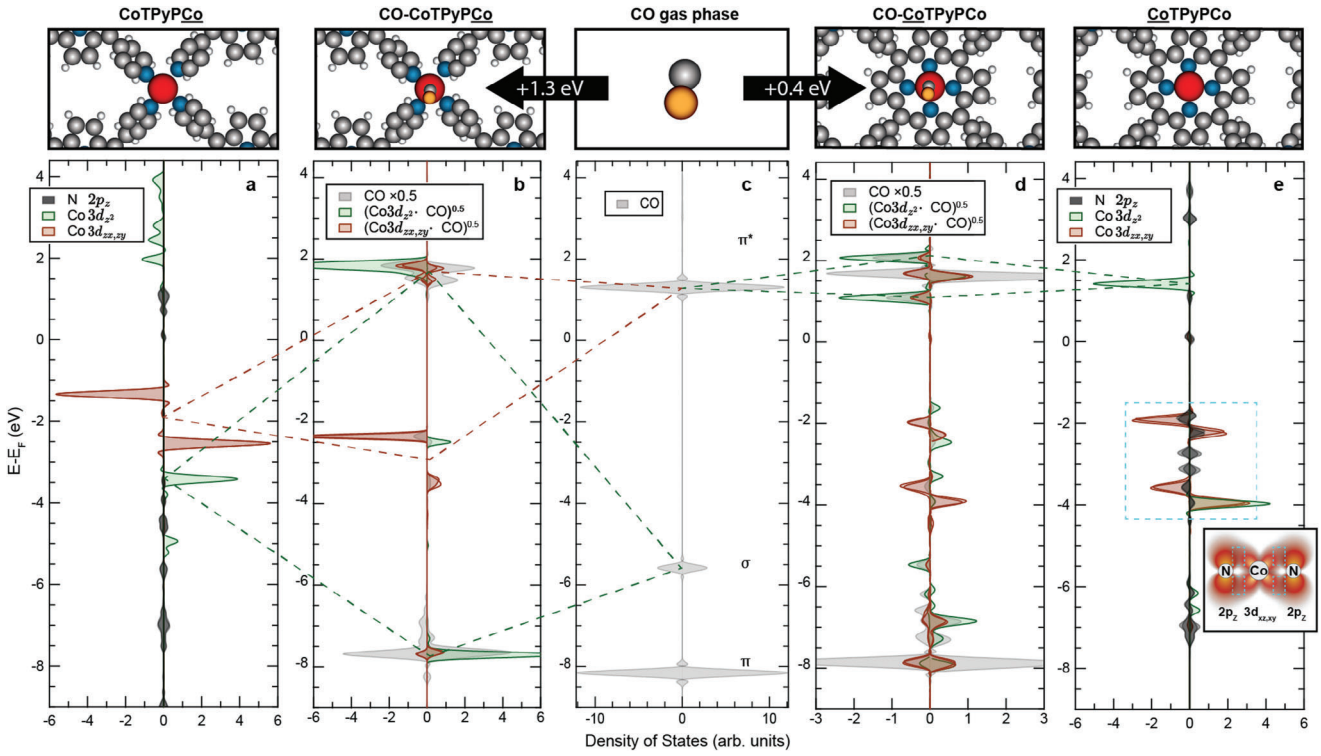

Figure 4. Calculated spin-polarized PDOS for CO ligation at the two non-equivalent CoTPyPCo cobalt sites. a) CoTPyP**Co** and the sum of the four coordinating N atoms; b) CO/CoTPyP**Co**; c) gas phase CO; d) CO/**Co**TPyPCo; e) **Co**TPyPCo and the sum of the four coordinating N atoms. The CO orbitals are calculated as the sum of all C and O orbitals. In (b) and (d), Co orbitals have been multiplied, separately for each spin channel, by the CO orbitals of the corresponding system: this allows us to better visualize the orbital overlap between Co and CO.

UHV conditions. Concerning the exact adsorption site, ligation of CO at the CoTPyP**Co** site, rather than at the **Co**TPyPCo site, is indicated by our DFT calculations, predicting an adsorption energy of 1.3 eV for the former cobalt species and of only 0.4 eV for the latter. To elucidate the origin of this difference, we carefully examined the calculated Projected Density of States (PDOS) curves shown in **Figure 4**. The PDOS curves not strictly necessary for the discussion below have been plotted separately in Figure S13 (Supporting Information). The CO states, together with Co $3d_{z^2}$ and $3d_{zx,zy}$ (the only orbitals involved in CO bonding), are plotted for both CoTPyP**Co** and **Co**TPyPCo sites, with and without the CO ligand, to facilitate comparison. For a clearer visualization of the Co hybridization with CO, Figures 4b,d display the product of Co $3d_{z^2}$ and $3d_{zx,zy}$ with the CO states, calculated separately for the two spin channels. In the case of CoTPyP**Co** (Figure 4b), bonding states at −7.5 and −2.5 eV for $3d_{z^2}$ and $3d_{zx,zy}$, respectively, are observed. Above the Fermi level, set as the zero reference, overlapped $3d_{z^2}$ and $3d_{zx,zy}$ antibonding states at 1.5 eV are also observed. If we consider the original orbitals (i.e., before ligation) in Figure 4a,c, the well-known Blyholder model applies, as the CO σ (HOMO) donates electrons to the Co $3d_{z^2}$, and its π^* (LUMO) accepts electrons from the fully occupied Co $3d_{zx,zy}$ (see dotted lines for guidance). In contrast, for the **Co**TPyPCo site, the $3d_{zx,zy}$ (Figure 4e inlay) orbital is already involved prior to CO ligation into covalent bonding with the four surrounding nitrogen atoms. Splitting of the $3d_{zx,zy}$ states, at −2.0 and −4.0 eV is observed, both overlapped with out-of-plane N $2p_z$, due to the two pairs of non-equivalent iminic N atoms caused by the saddle-shaped macrocycle distortion. The unavailable $3d_{zx,zy}$ atomic orbitals of **Co**TPyPCo make hybridization less effective, as no overlap is observed in Figure 4d. The Co—N bond lengths differ significantly between **Co**TPyPCo and CoTPyP**Co**: ≈1.9 Å in the former case, much larger (2.3 Å) in the latter, substantially reducing the overlap between Co and N orbitals. These values are consistent with similar systems, such as ZnTPyPFe/Au(111) where the observed Fe—N distance was also 2.3 Å.[71] Notably, the gas-phase simulation of the CoTPyPCo monolayer predicts a Co-pyridyl-N distance of only 1.99 Å.[24] This suggests that the presence of the support cannot be fully disregarded, even in the case of a weakly interacting substrate like graphene, where Van der Waals interactions, although weak, may play an essential role in determining the metal coordination distance in the SMON, the bond strength, the degree of orbital hybridization and, thus, the reactivity.

3. Conclusion

In this paper, we demonstrate that a Surface Confined Metal–Organic Network (SMON) formed upon a non-interacting graphene sheet can display metal centers with non-equivalent chemical activity. The SMON was synthesized by self-assembling a monolayer of CoTPyPs on Gr/Ir(111) in UHV conditions and by subsequent coordination of single Co adatoms with the pyridyl groups. The assembly of the CoTPyPCo coordination network induces a shift of ≈0.8 eV in the original electronic

molecular states. Notably, this shift is related to the Co loading of the network, representing a way to fine-tune its geometric and physicochemical properties. This model system allows us to investigate the nature of the long-range interactions inside the network on a non-perturbative support. The results reveal tuning of the macrocyclic **Co**TPyP oxidation state from +2 to +3 upon coordination with the Co ad-atoms, while the CoTPyP**Co** species exhibits an unusual +1 oxidation state. Thanks to its different bonding environment (despite the similar coordination) and electronic structure, the latter Co species promotes activation of CO, with a ligation energy of 1.3 eV. This is made possible by the fully occupied CoTPyP**Co** $3d_{zx,zy}$ orbitals, which are capable of π^* bonding with the LUMO of the CO axial ligand. In contrast, in **Co**TPyPCo, the shorter Co—N bond length leads to the hybridization of the same $3d_{zx,zy}$ orbitals with the surrounding N $2p_z$, selectively hindering the ligation of carbon monoxide. Within a more general picture, the stabilization at surfaces of the highly reactive +1 and high-valence +3 single metal atom oxidations states requires a strong role of the supporting interface in terms of charge transfer.[72–74] This makes the present case of particular interest, since the interactions that actually determine the charge states take place within the layer. Moreover, such a wide tunability range of the oxidation state is rare also in Nature, with cobalamin (vitamin B12) playing a unique role, being able to switch between the stable Co(III) to the radical Co(II) and to the nucleophilic Co(I) species.[75] However, the biochemical mechanism still exploits the molecular trans effect, implemented via homo- or hetero-lytic scission processes.[76]

4. Experimental Section

Sample Preparation: The sample has been prepared in UHV environments with base pressures of 1×10^{-10}mbar. The Ir(111) single crystal was cleaned by standard cycles of Ar^+ sputtering (E = 2 keV) and annealing @1200-1250 K, alternated with treatments in 1×10^{-7} mbar oxygen background in the 570–1100 K temperature range. Before growing Gr, the sample was finally annealed to 1250 K in UHV to desorb residual oxygen. Gr was grown by thermal decomposition of ethylene dosed from the background *in vacuo* following well-known recipes.[56,77] Graphene quality was checked by LEED (not shown), where no rotational domains could be observed and higher-order diffraction spots of the Gr moiré were visible. STM imaging of the bare Gr reveals hundreds of nanometer-wide graphene domains, with a defect density of the order of 0.01 nm^{-2}. The CoTPyP/Gr/Ir(111) layer was grown *in vacuo* by physical vapor deposition of the molecules on the Gr substrate. Cobalt tetra-pyridyl-porphyrin chloride molecules (CoTPyPCl = 5,10,15,20-tetra(4-pyridyl)21H,23H-porphyrin Co(III) chloride) were purchased from Frontier Scientific. The molecular source was a heated boron nitride crucible. The typical deposition rate was of the order of 0.03ML $mi^{-1}n$ and was calibrated by means of a quartz microbalance. In order to remove the residual organic contaminants and the Cl ligand, the molecules have been kept at 500 K nightlong for proper outgassing. The CoTPyP deposition on Gr/Ir(111) was done with the sample kept at 500 K and a crucible temperature of ≈600 K, in a residual background pressure of 5×10^{-10}mbar. The chloride ligand, which guarantees the chemical stability of the porphyrin in air, detaches from the molecule in the evaporation process.[9,78,79] The CoTPyPCo layer was formed upon post-deposition of single Co ad-atoms by thermal sublimation from a resistively heated pure cobalt filament, with the substrate kept at 400 K for best ordering and to avoid Co intercalation under graphene.[80] Only for ARPES measurements a commercial metal-evaporator using a Co-rod heated by electron bombardment and provided with a flux monitor (calibrated with XPS) was employed. In all cases, the typical deposition rate was of the order of 0.1 ML $mi^{-1}n$, checked with Auger Electron Spectroscopy (AES) or XPS, depending on the setup, keeping graphene as a reference.

STM-STS: STM-STS measurements were performed using a commercial Omicron Low-Temperature STM based at CNR – Istituto Officina dei Materiali (IOM), Trieste, Italy, brought to a temperature of 77 K. STS spectra and maps were acquired with a lock-in amplifier set to modulate the bias with a sine wave of amplitude 20 mV and frequency 1090 Hz. dI/dV spectra were divided by I/V and recalibrated in order to match the numerical derivative of I/V. All images were post-processed with Gwyddion software.

IR-VIS SFG: IR-Vis Sum Frequency Generation vibronic spectroscopy is a nonlinear optical technique.[81,82] The measurements were performed in a dedicated setup at the Department of Physics of the University of Trieste.[50] A UHV system with a base pressure of 5×10^{-11} mbar hosting standard surface science preparation and characterization techniques is directly coupled with a high-pressure cell for in situ IR–vis SFG spectroscopy (base pressure better than 5×10^{-9} mbar). The reactor is equipped with a gas system to handle the reactants' pressure in the 10^{-9}–10^{+3} mbar range. The inlet and outlet of the laser beams are provided by UHV- compatible BaF_2 windows. The excitation source (Ekspla, 1064 nm, 30 ps, 50 Hz) delivers a 532 nm (2.33 eV) second harmonic visible beam and IR radiation, tunable in 1000–4500 cm^{-1} range, obtained thanks to harmonic and parametric generation. The raw spectra are normalized to the impinging IR and Vis excitation intensities, and then to a reference spectrum of clean Au. The normalized SFG spectra were then analyzed by least-squares fitting to a parametric, effective expression of the nonlinear second-order susceptibility.[81,83] The following expression well reproduces the observed lineshapes, accounting for the resonant IR-Vis vibronic transitions and the non-resonant background, and describing all the interference terms.

$$\frac{I_{SFG}(\omega_{IR})}{I_{VIS} I_{IR}(\omega_{IR})} \propto \left| A_{NRes} + \sum_k \frac{A_k e^{i\Delta\Phi k}}{\omega_{IR} - \omega_k + i\Gamma_k} \right|^2 \quad (2)$$

A_{NRes} and A_k account for the amplitudes of the non-resonant and kth-resonant contributions, respectively. $\Delta\Phi_k$ is the phase difference between the kth-resonant and non-resonant signals. ω_k is the energy position of the line and Γ_k the Lorentzian broadening, related to the dephasing rate, which in turn stems from the energy lifetime and the elastic dephasing of the excited vibronic state.[84] In Figure 3, the normalized IR–vis SFG signal intensity (dots) was plotted, together with the best fit (lines) and the deconvolution of each *k*-resonance with its interference with the non-resonant background (color-filled profiles). The latter are calculated with the parameters obtained from the fitting procedure following:

$$\frac{I_{SFG,k}(\omega_{IR})}{I_{VIS} I_{IR}(\omega_{IR})} \frac{I_{SFG,k}(\omega_{IR})}{I_{VIS} I_{IR}(\omega_{IR})} \propto \left| A_{NRes} + \frac{A_k e^{i\Delta\Phi k}}{\omega_{IR} - \omega_k + i\Gamma k} \right|^2 \quad (3)$$

These plots interestingly put in direct evidence the amplitude and the relative phase for each of the resonances. Further details and examples can be found in the previous works.[50,61] In the present study, all spectra were collected in the ppp polarization configuration (SFG-visible-infrared).

DFT: DFT calculations were performed with the pseudopotential plane wave code Quantum ESPRESSO.[85–87] Both CoTPyP and CoTPyPCo systems were described using periodic boundary conditions in an oblique lattice modeled with in-plane lattice parameters and angles, respectively, of a = 30.97 Å, b = 14.84 Å and $\alpha = 63.8°$ and a = 28.36 Å, b = 20.23 Å and $\alpha = 44.9°$, containing two molecules and a Gr layer composed of 156 and 140 C atoms, respectively. In order to reduce the computational cost, the Ir(111) substrate was neglected due to its weak interaction with Gr. To avoid the use of bigger coincidence cells, the Gr lattice was slightly stretched. For CoTPyP a Gr lattice parameter of 2.47 Å was used, while for CoTPyPCo an asymmetric stretch was applied on Gr, corresponding to a Gr unit cell with in-plane parameters a = 2.48 Å, b = 2.53 Å, $\alpha = 61.3°$. Spin-polarized calculations were carried

out using the Perdew-Burke-Ernzewrhof (PBE) exchange-correlation functional within the generalized gradient approximation (GGA) method.[88] Vanderbilt ultrasoft pseudopotentials[89] were employed except for Co atoms, for which the Rappe-Rabe-Kaxiras-Joannopoulos (RRKJ) ultrasoft pseudopotential[89] was used. The Hubbard-U correction[90] was introduced to improve the description of the metal atoms 3d states, with a parameter U = 3.5 eV for Co chosen in order to reproduce the 5.5 eV energy gap between occupied and unoccupied $3d_{z^2}$ levels reported in literature.[91] Van der Waals interactions were also included using the Grimme-D3 approach.[92] The plane-wave cutoffs of 60 Ry and 240 Ry were employed for the wave function and the charge density respectively. The Methfessel-Paxton smearing scheme was used for the occupation of electronic states with a smearing parameter of 0.01 Ry.[93] Geometrical optimizations were carried out using the Broyden-Fletcher-Goldfarb-Shanno algorithm with energies and forces convergence thresholds of 1×10^{-6} Ry for the whole cell and 1×10^{-3} a.u. for each atomic force component, respectively. For the reciprocal space sampling, uniform grids of $2 \times 4 \times 1$ and $4 \times 8 \times 1$ k-points were employed respectively for self-consistent field (SCF) and non-self-consistent field (NSCF) calculations. The STM and STS simulations were performed in a Tersoff-Hamann approach,[94] assuming a constant density of states for the tip. For STM images the integration range for the electronic density corresponds to the applied bias. Oxidation states for the Co metal center were determined according to the literature,[95] counting the number of valence electrons to be assigned to the atom as the number of its fully occupied 3d orbitals (i.e., Löwdin population of the orbital equal to 1).

XPS, UPS, and 2PPE: XPS, UPS, and 2PPE spectroscopies were performed at the ANCHOR-SUNDYN laboratory[96] at CNR – Istituto Officina dei Materiali (IOM), Trieste (Italy). XPS spectra were recorded using a monochromatized Al K_α source with the analyzer (SPECS Phoibos 150) pass energy set to 50 eV. UPS was performed by acquiring either the HeII or the HeI spectra: in the latter case, a −2.5 V bias was applied to the sample in order to detect the secondary electron cutoff and measure the sample work function (Figure S10, Supporting Information). For time-resolved 2PPE measurements, the fundamental output of a Yb-doped yttrium aluminum garnet (Yb:YAG) laser was split to generate the frequency quadrupled probe beam (257 nm, 4.82 eV) and to feed an optical parametric amplifier (OPA), delivering the pump beam. For this experiment, the excitation wavelength was tuned to 532 nm (2.33 eV) to match the photon energy of the visible pulses of the SFG setup.

ARPES: The ARPES measurements have been performed at the NanoESCA beamline of Elettra, the Italian synchrotron radiation facility, using a FOCUS NanoESCA photoemission electron microscope (PEEM).[97] In the PEEM the photoelectron signal is collected from a spot size of ≈5–10 µm. Before the experiment, the sample was prepared according to the procedure described above. The measurements were conducted with a photon energy of 35 eV and an overall energy resolution of 50 meV using p-polarized synchrotron radiation while keeping the sample at 90 K.

Supporting Information

Supporting Information is available from the Wiley Online Library or from the author.

Acknowledgements

This project was funded by Unione Europea – Next Generation EU through projects PRIN2022 XXJNRS 2DOrNotToBe and PRIN PNRR P2022B3WCB 2Dgo3D. The authors thank B. Busson for fruitful discussions about the IR–vis SFG non-resonant background. M.P. acknowledges support from the Fondazione ICSC "Italian Research Center on High-Performance Computing, Big Data, and Quantum Computing" – Spoke 7, Materials and Molecular Sciences – National Recovery and Resilience Plan (PNRR) – funded by MUR Missione 4 – Componente 2 – Investimento 1.4 – Next Generation EU (NGEU). Computational resources were obtained from CINECA through the ISCRA initiative and the agreement with the University of Trieste.

Open access publishing facilitated by Universita degli Studi di Trieste, as part of the Wiley - CRUI-CARE agreement.

Conflict of Interest

The authors declare no conflict of interest.

Author Contributions

E.V. supervised the project, conceived, designed the experiments and edited the final version of the manuscript. F.A. performed all the experiments and analyzed the data. A.S. participated in the STM/STS experiment. R.C., M.D.A., and S.B. took part in the XPS, UPS, and tr-2PPE experiments with the respective data analyses. I.C. and V.F. participated in the ARPES experiment. S.B. assisted with the SFG measurements. D.B. performed all the DFT calculations under the supervision of M.P. F.A. and E.V. wrote the initial draft of the manuscript with input from all authors. All authors contributed to the scientific discussion and edited the final version of the manuscript.

Data Availability Statement

The data that support the findings of this study are available from the corresponding author upon reasonable request.

Keywords

2D coordination network, cobalt, graphene, metal–organic network, oxidation state, porphyrin

Received: May 13, 2024
Revised: July 24, 2024
Published online: August 14, 2024

[1] L. Dong, Z. A. Gao, N. Lin, *Prog. Surf. Sci.* **2016**, *91*, 101.
[2] Y. Li, J. Xiao, T. E. Shubina, M. Chen, Z. Shi, M. Schmid, H.-P. P. Steinrück, J. M. Gottfried, N. Lin, *J. Am. Chem. Soc.* **2012**, *134*, 6401.
[3] M. DeJong, A. J. A. Price, E. Mårsell, G. Tom, G. D. Nguyen, E. R. Johnson, S. A. Burke, *Nat. Commun.* **2022**, *13*, 7407.
[4] H. Lv, X. Li, D. Wu, Y. Liu, X. Li, X. Wu, J. Yang, *Nano Lett.* **2022**, *22*, 1573.
[5] E. Vesselli, *Journal of Physics: Materials* **2020**, *3*, 022002.
[6] E. Vesselli, *Nanoscale Advances* **2021**, *3*, 1319.
[7] X. M. Hu, M. H. Rønne, S. U. Pedersen, T. Skrydstrup, K. Daasbjerg, *Angew. Chem. – Int. Ed.* **2017**, *56*, 6468.
[8] P. K. Sonkar, K. Prakash, M. Yadav, V. Ganesan, M. Sankar, R. Gupta, D. K. Yadav, *J. Mater. Chem. A* **2017**, *5*, 6263.
[9] B. Wurster, D. Grumelli, D. Hötger, R. Gutzler, K. Kern, *J. Am. Chem. Soc.* **2016**, *138*, 3623.
[10] I. Azcarate, C. Costentin, M. Robert, J. M. Savéant, *J. Am. Chem. Soc.* **2016**, *138*, 16639.
[11] E. M. Nichols, J. S. Derrick, S. K. Nistanaki, P. T. Smith, C. J. Chang, *Chem. Sci.* **2018**, *9*, 2952.
[12] Y. Feng, N. Alonso-Vante, *Physica Status Solidi (B) Basic Research* **2008**, *245*, 1792.
[13] M. Bevilacqua, J. Filippi, A. Lavacchi, A. Marchionni, H. A. Miller, W. Oberhauser, E. Vesselli, F. Vizza, *Energy Technol.* **2014**, *2*, 522.
[14] W. Auwärter, D. Écija, F. Klappenberger, J. V. Barth, *Nat. Chem.* **2015**, *7*, 105.

[15] J. M. Gottfried, *Surf. Sci. Rep.* **2015**, *70*, 259.
[16] R. Hou, Y. Guo, Z. Yi, Z. Zhang, C. Zhang, W. Xu, *J. Phys. Chem. Lett.* **2023**, *14*, 3636.
[17] T. Lin, G. Kuang, W. Wang, N. Lin, *ACS Nano* **2014**, *8*, 8310.
[18] T. Lin, X. S. Shang, J. Adisoejoso, P. N. Liu, N. Lin, *J. Am. Chem. Soc.* **2013**, *135*, 3576.
[19] J.-C. Dong, M. Su, V. Briega-Martos, L. Li, J.-B. Le, P. Radjenovic, X.-S. Zhou, J. M. Feliu, Z.-Q. Tian, J.-F. Li, *J. Am. Chem. Soc.* **2020**, *142*, 715.
[20] D. Fa, Y. Tao, X. Pan, D. Wang, G. Feng, J. Yuan, *Angew. Chem. Int. Ed.* **2022**, *61*, 202207845.
[21] M. El Garah, A. Ciesielski, N. Marets, V. Bulach, M. W. Hosseini, P. Samorì, *Chem. Commun.* **2014**, *50*, 12250.
[22] G. Rupprechter, C. Weilach, *Nano Today* **2007**, *2*, 20.
[23] M. Corva, A. Ferrari, M. Rinaldi, Z. Feng, M. Roiaz, C. Rameshan, G. Rupprechter, R. Costantini, M. Dell'Angela, G. Pastore, G. Comelli, N. Seriani, E. Vesselli, *Nat. Commun.* **2018**, *9*, 4703.
[24] B. Mandal, J. S. Chung, S. G. Kang, *J. Phys. Chem. C* **2018**, *122*, 9899.
[25] W. Hieringer, K. Flechtner, A. Kretschmann, K. Seufert, W. Auwärter, J. V. Barth, A. Görling, H.-P. Steinrück, J. M. Gottfried, *J. Am. Chem. Soc.* **2011**, *133*, 6206.
[26] H. Peisert, J. Uihlein, F. Petraki, T. Chassé, *J. Electron Spectrosc. Relat. Phenom.* **2015**, *204*, 49.
[27] A. P. Seitsonen, M. Lingenfelder, H. Spillmann, A. Dmitriev, S. Stepanow, N. Lin, K. Kern, J. V. Barth, *J. Am. Chem. Soc.* **2006**, *128*, 5634.
[28] Y. Gurdal, J. Hutter, M. Iannuzzi, *J. Phys. Chem. C* **2017**, *121*, 11416.
[29] F. Armillotta, A. Pividori, M. Stredansky, N. Seriani, E. Vesselli, *Top. Catal.* **2020**, *63*, 1585.
[30] K. Zhou, H. Liang, M. Wang, S. Xing, H. Ding, Y. Song, Y. Wang, Q. Xu, J. H. He, J. Zhu, W. Zhao, Y. Q. Ma, Z. Shi, *Nanoscale Advances* **2020**, *2*, 2170.
[31] J. Amanpour, G. Hu, E. J. Alexy, A. K. Mandal, H. S. Kang, J. M. Yuen, J. R. Diers, D. F. Bocian, J. S. Lindsey, D. Holten, *J. Phys. Chem. A* **2016**, *120*, 7434.
[32] Q. Liu, X. Zhang, W. Zeng, J. Wang, Z. Zhou, *J. Phys. Chem. B* **2015**, *119*, 14102.
[33] Y. Wang, X.-P. Zhang, H. Lei, K. Guo, G. Xu, L. Xie, X. Li, W. Zhang, U.-P. Apfel, R. Cao, *CCS Chem* **2022**, *4*, 2959.
[34] I. Cojocariu, S. Carlotto, G. Zamborlini, M. Jugovac, L. Schio, L. Floreano, M. Casarin, V. Feyer, C. M. Schneider, *J. Mater. Chem. C* **2021**, *9*, 12559.
[35] J. E. Pander, A. Fogg, A. B. Bocarsly, *ChemCatChem* **2016**, *8*, 3536.
[36] N. Kornienko, Y. Zhao, C. S. Kley, C. Zhu, D. Kim, S. Lin, C. J. Chang, O. M. Yaghi, P. Yang, *J. Am. Chem. Soc.* **2015**, *137*, 14129.
[37] L. C. Grabow, B. Hvolbæk, J. K. Nørskov, *Top. Catal.* **2010**, *53*, 298.
[38] P. Ebrahimi, A. Kumar, M. Khraisheh, *Emergent Materials* **2020**, *3*, 881.
[39] H. Toulhoat, P. Raybaud, *Catalysis Science and Technology* **2020**, *10*, 2069.
[40] D. Bidoggia, F. Armillotta, A. Sala, E. Vesselli, M. Peressi, *J. Phys. Chem. C* **2024**, *128*, 1737.
[41] B. D. Baker Cortés, M. Enache, K. Küster, F. Studener, T. L. Lee, N. Marets, V. Bulach, M. W. Hosseini, M. Stöhr, *Chemistry – A European Journal* **2021**, *27*, 12430.
[42] F. Buchner, I. Kellner, W. Hieringer, A. Görling, H.-P. Steinrück, H. Marbach, *Phys. Chem. Chem. Phys.* **2010**, *12*, 13082.
[43] A. Stein, D. Rolf, C. Lotze, C. Czekelius, K. J. Franke, P. Tegeder, *J. Phys.: Condens. Matter* **2019**, *31*, 044002.
[44] K. Seufert, M. L. Bocquet, W. Auwärter, A. Weber-Bargioni, J. Reichert, N. Lorente, J. V. Barth, *Nat. Chem.* **2011**, *3*, 114.
[45] H. Sheng, J. Wang, J. Huang, Z. Li, G. Ren, L. Zhang, L. Yu, M. Zhao, X. Li, G. Li, N. Wang, C. Shen, G. Lu, *Nat. Commun.* **2023**, *14*, 1528.
[46] S. Yoshimoto, A. Tada, K. Suto, R. Narita, K. Itaya, *Langmuir* **2003**, *19*, 672.
[47] B. Liu, S. Zhang, G. Miao, J. Guo, S. Meng, W. Wang, *Chem. Commun.* **2021**, *57*, 4580.
[48] D. Ranieri, A. Privitera, F. Santanni, K. Urbanska, G. J. Strachan, B. Twamley, E. Salvadori, Y. Liao, M. Chiesa, M. O. Senge, F. Totti, L. Sorace, R. Sessoli, *Angew. Chem., Int. Ed.* **2023**, 62.
[49] W. Li, L. Sun, J. Qi, P. Jarillo-Herrero, M. Dincă, J. Li, *Chem. Sci.* **2017**, *8*, 2859.
[50] F. Armillotta, D. Bidoggia, S. Baronio, P. Biasin, A. Annese, M. Scardamaglia, S. Zhu, B. Bozzini, S. Modesti, M. Peressi, E. Vesselli, *ACS Catal.* **2022**, *12*, 7950.
[51] Y. Bai, M. Sekita, M. Schmid, T. Bischof, H.-P. Steinrück, J. M. Gottfried, *Phys. Chem. Chem. Phys.* **2010**, *12*, 4336.
[52] O. Gunnarsson, K. Schönhammer, *Phys. Rev. Lett.* **1978**, *41*, 1608.
[53] T. Lukasczyk, K. Flechtner, L. R. Merte, N. Jux, F. Maier, J. M. Gottfried, H.-P. Steinrück, *J. Phys. Chem. C* **2007**, *111*, 3090.
[54] A. Sala, G. Zamborlini, T. O. Menteş, A. Locatelli, *Small* **2015**, *11*, 5927.
[55] R. Larciprete, S. Ulstrup, P. Lacovig, M. Dalmiglio, M. Bianchi, F. Mazzola, L. Hornekær, F. Orlando, A. Baraldi, P. Hofmann, S. Lizzit, *ACS Nano* **2012**, *6*, 9551.
[56] I. Pletikosić, M. Kralj, P. Pervan, R. Brako, J. Coraux, A. T. N'Diaye, C. Busse, T. Michely, A. T. N'Diaye, C. Busse, T. Michely, *Phys. Rev. Lett.* **2009**, *102*, 056808.
[57] G. Giovannetti, P. A. Khomyakov, G. Brocks, V. M. Karpan, J. Van Den Brink, P. J. Kelly, *Phys. Rev. Lett.* **2008**, *101*, 4.
[58] G. Zamborlini, D. Lüftner, Z. Feng, B. Kollmann, P. Puschnig, C. Dri, M. Panighel, G. Di Santo, A. Goldoni, G. Comelli, M. Jugovac, V. Feyer, C. M. Schneidery, *Nat. Commun.* **2017**, *8*, 335.
[59] M. Jugovac, C. Tresca, I. Cojocariu, G. Di Santo, W. Zhao, L. Petaccia, P. Moras, G. Profeta, F. Bisti, G. Di Santo, W. Zhao, L. Petaccia, P. Moras, G. Profeta, F. Bisti, *Phys. Rev. B* **2022**, *105*, L241107.
[60] C. Tusche, M. Ellguth, V. Feyer, A. Krasyuk, C. Wiemann, J. Henk, C. M. Schneider, J. Kirschner, *Nat. Commun.* **2018**, 9.
[61] M. Corva, F. Mohamed, E. Tomsic, M. Rinaldi, C. Cepek, N. Seriani, M. Peressi, E. Vesselli, *J. Phys. Chem. C* **2019**, *123*, 3916.
[62] K. Araki, P. S. Santos, L. F. C. C. de Oliveira, H. E. Toma, *Spectrosc. Lett.* **1995**, *28*, 119.
[63] N. Blom, J. Odo, K. Nakamoto, D. P. Strommen, *Journal of Physical Chemistry* **1986**, *90*, 2847.
[64] S. Popovici, W. Leyffer, R. Holze, *J. Porphyrins Phthalocyanines* **1998**, *02*, 249.
[65] M. Aydin, *Vib. Spectrosc.* **2013**, *68*, 141.
[66] L. Dalstein, A. Revel, C. Humbert, B. Busson, *J. Chem. Phys.* **2018**, 148.
[67] B. Busson, L. Dalstein, *J. Chem. Phys.* **2018**, 149.
[68] B. Busson, L. Dalstein, *J. Chem. Phys.* **2018**, *149*, 154701.
[69] C. Hess, M. Bonn, S. Funk, M. Wolf, *Chem. Phys. Lett.* **2000**, *325*, 139.
[70] V. L. Zhang, H. Arnolds, D. A. King, *Surf. Sci.* **2005**, *587*, 102.
[71] B. D. Baker Cortés, N. Schmidt, M. Enache, M. Stöhr, *J. Phys. Chem. C* **2021**, *125*, 24557.
[72] G. Zamborlini, M. Jugovac, A. Cossaro, A. Verdini, L. Floreano, D. Lüftner, P. Puschnig, V. Feyer, C. M. Schneider, *Chem. Commun.* **2018**, *54*, 13423.
[73] J. Herritsch, M. Zugermeier, M. Schmid, M. Chen, J.-N. Luy, P. Schweyen, M. Bröring, R. Tonner-Zech, J. M. Gottfried, *J. Porphyrins Phthalocyanines* **2023**, *27*, 670.
[74] P. S. Deimel, P. C. Aguilar, M. Paszkiewicz, D. A. Duncan, J. V. Barth, F. Klappenberger, W. Schöfberger, F. Allegretti, *Chem. Commun.* **2020**, *56*, 11219.
[75] M. Giedyk, K. Goliszewska, D. Gryko, *Chem. Soc. Rev.* **2015**, *44*, 3391.
[76] L. Randaccio, S. Geremia, N. Demitri, J. Wuerges, *Molecules* **2010**, *15*, 3228.

[77] J. Coraux, A. T. N'Diaye, M. Engler, C. Busse, D. Wall, N. Buckanie, F.-J. Meyer zu Heringdorf, R. van Gastel, B. Poelsema, T. Michely, *New J. Phys.* **2009**, *11*, 023006.
[78] B. E. Murphy, S. A. Krasnikov, N. N. Sergeeva, A. A. Cafolla, A. B. Preobrajenski, A. N. Chaika, O. Lübben, I. V. Shvets, *ACS Nano* **2014**, *8*, 5190.
[79] F. Armillotta, D. Bidoggia, P. Biasin, A. Annese, A. Cossaro, A. Verdini, L. Floreano, M. Peressi, E. Vesselli, *Cell Reports Physical Science* **2023**, *4*, 101378.
[80] R. Decker, J. Brede, N. Atodiresei, V. Caciuc, S. Blügel, R. Wiesendanger, *Physical Review B – Condensed Matter and Materials Physics* **2013**, *87*, 041403.
[81] C. S. Tian, Y. R. Shen, *Surf. Sci. Rep.* **2014**, *69*, 105.
[82] Y. R. Shen, *Nature* **1989**, *337*, 519.
[83] M. Hayashi, S. H. Lin, M. B. Raschke, Y. R. Shen, *The Journal of Physical Chemistry A* **2002**, *106*, 2271.
[84] M. Bonn, C. Hess, W. G. Roeterdink, H. Ueba, M. Wolf, *Chem. Phys. Lett.* **2004**, *388*, 269.
[85] P. Giannozzi, S. Baroni, N. Bonini, M. Calandra, R. Car, C. Cavazzoni, D. Ceresoli, G. L. Chiarotti, M. Cococcioni, I. Dabo, A. Dal Corso, S. de Gironcoli, S. Fabris, G. Fratesi, R. Gebauer, U. Gerstmann, C. Gougoussis, A. Kokalj, M. Lazzeri, L. Martin-Samos, N. Marzari, F. Mauri, R. Mazzarello, S. Paolini, A. Pasquarello, L. Paulatto, C. Sbraccia, S. Scandolo, G. Sclauzero, A. P. Seitsonen, et al., *J. Phys.: Condens. Matter* **2009**, *21*, 395502.
[86] P. Giannozzi, O. Andreussi, T. Brumme, O. Bunau, M. Buongiorno Nardelli, M. Calandra, R. Car, C. Cavazzoni, D. Ceresoli, M. Cococcioni, N. Colonna, I. Carnimeo, A. Dal Corso, S. de Gironcoli, P. Delugas, R. A. DiStasio, A. Ferretti, A. Floris, G. Fratesi, G. Fugallo, R. Gebauer, U. Gerstmann, F. Giustino, T. Gorni, J. Jia, M. Kawamura, H.-Y. Ko, A. Kokalj, E. Küçükbenli, M. Lazzeri, et al., *J. Phys.: Condens. Matter* **2017**, *29*, 465901.
[87] P. Giannozzi, O. Baseggio, P. Bonfà, D. Brunato, R. Car, I. Carnimeo, C. Cavazzoni, S. de Gironcoli, P. Delugas, F. Ferrari Ruffino, A. Ferretti, N. Marzari, I. Timrov, A. Urru, S. Baroni, *J. Chem. Phys.* **2020**, *152*, 154105.
[88] J. P. Perdew, K. Burke, M. Ernzerhof, *Phys. Rev. Lett.* **1996**, *77*, 3865.
[89] D. Vanderbilt, *Phys. Rev. B* **1990**, *41*, 7892.
[90] M. Cococcioni, S. de Gironcoli, *Phys. Rev. B* **2005**, *71*, 035105.
[91] L. G. G. V. Dias da Silva, M. L. Tiago, S. E. Ulloa, F. A. Reboredo, E. Dagotto, *Phys. Rev. B* **2009**, *80*, 155443.
[92] S. Grimme, J. Antony, S. Ehrlich, H. Krieg, *J. Chem. Phys.* **2010**, *132*, 154104.
[93] M. Methfessel, A. T. Paxton, *Phys. Rev. B* **1989**, *40*, 3616.
[94] J. Tersoff, D. R. Hamann, *Phys. Rev. B* **1985**, *31*, 805.
[95] P. H. L. Sit, R. Car, M. H. Cohen, A. Selloni, *Inorg. Chem.* **2011**, *50*, 10259.
[96] R. Costantini, M. Stredansky, D. Cvetko, G. Kladnik, A. Verdini, P. Sigalotti, M. D. Angela, F. Cilento, F. Salvador, A. De Luisa, D. Benedetti, L. Floreano, A. Morgante, A. Cossaro, M. Dell'Angela, *J. Electron Spectrosc. Relat. Phenom.* **2018**, *229*, 7.
[97] C. M. Schneider, C. Wiemann, M. Patt, V. Feyer, L. Plucinski, I. P. Krug, M. Escher, N. Weber, M. Merkel, O. Renault, N. Barrett, *J. Electron Spectrosc. Relat. Phenom.* **2012**, *185*, 330.